

Article

Cavitation Inception on Hydrokinetic Turbine Blades Shrouded by Diffuser

Hamilton Pessoa Picanço *, Adry Kleber Ferreira de Lima, Déborah Aline Tavares Dias do Rio Vaz, Erb Ferreira Lins and Jerson Rogério Pinheiro Vaz 

Engineering of Natural Resources of the Amazon Graduate Program (PRODERNA), Institute of Technology, Federal University of Pará, Av. Augusto Correa, N 1, Belém 66075-900, PA, Brazil; adry@ufpa.br (A.K.F.d.L.); deborah.rio@gmail.com (D.A.T.d.R.V.); erb@ufpa.br (E.F.L.); jerson@ufpa.br (J.R.P.V.)

* Correspondence: hppicanco@ufpa.br

Abstract: Diffuser technology placed around hydrokinetic rotors may improve the conversion of the fluid's kinetic energy into shaft power. However, rotor blades are susceptible to the phenomenon of cavitation, which can impact the overall power efficiency. This paper presents the development of a new optimization model applied to hydrokinetic blades shrouded by a diffuser. The proposed geometry optimization takes into account the effect of cavitation inception. The main contribution of this work to the state of the art is the development of an optimization procedure that takes into account the effects of diffuser efficiency, η_d , and thrust, C_{Td} . The authors are unaware of any other work available in the literature considering the effect of η_d and C_{Td} on the cavitation of shrouded hydrokinetic blades. The model uses the Blade Element Momentum Theory to seek optimized blade geometry in order to minimize or even avoid the occurrence of cavitation. The minimum pressure coefficient is used as a criterion to avoid cavitation inception. Additionally, a Computational Fluid Dynamics investigation was carried out to validate the model based on the Reynolds-Averaged Navier–Stokes formulation, using the $\kappa - \omega$ Shear-Stress Transport turbulence and Rayleigh–Plesset models, to estimate cavitation by means of water vapor production. The methodology was applied to the design of a 10 m diameter hydrokinetic rotor, rated at 250 kW of output power at a flow velocity of 2.5 m/s. An analysis of the proposed model with and without a diffuser was carried out to evaluate the changes in the optimized geometry in terms of chord and twist angle distribution. It was found that the flow around a diffuser-augmented hydrokinetic blade doubles the cavitation inception relative to the unshrouded case. Additionally, the proposed optimization model can completely remove the cavitation occurrence, making it a good alternative for the design of diffuser-augmented hydrokinetic blades free of cavitation.



Citation: Picanço, H.P.; Kleber Ferreira de Lima, A.; Dias do Rio Vaz, D.A.T.; Lins, E.F.; Pinheiro Vaz, J.R. Cavitation Inception on Hydrokinetic Turbine Blades Shrouded by Diffuser. *Sustainability* **2022**, *14*, 7067. <https://doi.org/10.3390/su14127067>

Academic Editor: Zhengwei Wang

Received: 27 March 2022

Accepted: 12 May 2022

Published: 9 June 2022

Publisher's Note: MDPI stays neutral with regard to jurisdictional claims in published maps and institutional affiliations.



Copyright: © 2022 by the authors. Licensee MDPI, Basel, Switzerland. This article is an open access article distributed under the terms and conditions of the Creative Commons Attribution (CC BY) license (<https://creativecommons.org/licenses/by/4.0/>).

Keywords: diffuser; hydrokinetic turbine; cavitation; blade optimization; blade element momentum theory; Rayleigh–Plesset model

1. Introduction

Hydrokinetic turbines are attractive renewable technologies as they can harness the kinetic energy from rivers, estuaries, tidal and marine currents and convert it into electricity. The technological challenges of hydrokinetic and wind turbines are similar from a theoretical point of view. The classical Betz limit states that a maximum power coefficient of 16/27 for bare turbines in idealized flow conditions [1,2]. However, diffuser-augmented hydrokinetic turbines (DAHTs) can even overcome this limitation with a properly designed shroud that increases the mass flow over the rotor blades, improving power output. On the other hand, as the axial fluid velocity increases, cavitation reduces the advantage of the diffuser due to the appearance of cavitation bubbles. The development of non-cavitating blades for DAHTs is indeed important for the renewable energy industry, as it contributes to the efficient design of hydrokinetic turbines.

Although many papers have recently reported the use of diffusers on hydrokinetic or tidal turbines [3–5], only a few have established the implementation of optimized design of non-cavitating blades with a diffuser. For example, in [5], an optimization methodology for diffuser-augmented hydrokinetic blades free of cavitation was developed. Their work shows that cavitation is indeed sensitive to the diffuser speed-up ratio, and such a phenomenon needs to be considered in the design of shrouded hydrokinetic blades. However, no mention was made of diffuser efficiency, η_d , and thrust, C_{Td} .

In [6], the Blade Element Momentum Theory (BEMT) for the hydrodynamic design of marine current turbines was implemented. In that model, an investigation was carried out considering cavitation on shallow tip immersion. It was found that cavitation can be avoided with the suitable design of 2D blade sections. Although the work presented some interesting thoughts about cavitation, studies on optimization of hydrokinetic blades free of cavitation were not addressed.

In [7], supported by a Computational Fluid Dynamics (CFD) investigation, an optimization approach based on BEMT for horizontal axis hydrokinetic turbines, taking into account the effect of cavitation, was developed. The model was applied only to bare turbines, using the minimum pressure coefficient as a criterion in the optimization model. The research demonstrated that by modifying the blade geometry, the cavitation inception can be reduced even further.

In [5], the authors extended the optimization model presented in [2]. They developed a cavitation criterion for hydro turbines. Additionally, this work used the minimum pressure coefficient as a criterion to maintain the tip pressure above water vapor pressure, including the diffuser effect. To obtain the blade-optimized geometry, the chord is determined using the diffuser speed-up ratio as the manipulated variable to assess the corrected chord and twist angle for each blade section. The diffuser thrust and efficiency are not considered in the procedure.

As such, in wind turbines, the enhancement of DAHT's performance depends on the diffuser and rotor geometries. In the case of diffusers, the design parameters are inlet and outlet diameters, length, entrance angle, efficiency, area ratio and thrust coefficient. The last three parameters influence the turbine performance, but the authors are unaware of any work in the current literature showing the impact of them regarding cavitation. The concept of a good design for a DAHT must consider the effects of each of these parameters on the DAHT performance.

Cavitation may lead to a decrease in the hydrodynamic performance of a hydrokinetic rotor since pulses or fluctuations in local pressure significantly contribute to vapor bubble formation, also causing noise, vibrations and erosion of the blades [8–10]. Several CFD methods have been developed in recent decades to numerically investigate cavitation. Liquid and vapor are often treated as an homogeneous mixture with variable densities. This two-phase method uses an empirical transfer equation for the local volume fraction, and the interaction between water and vapor can be computed. In [11], the authors investigated two-dimensional sheet cavitation of three different mass transfer models for cavitating flows around hydrofoils, including the Zwart model, also in ANSYS/CFX. They applied an optimization strategy to properly tune the empirical coefficients of each model. They concluded that the results were nearly the same for the three models, in good agreement with experiments.

Different dynamics of cavitating behaviors can be observed in liquid flows. According to [12], incipient cavitation, shear cavitation, sheet/cloud cavitation and supercavitation regimes can be found depending on the nondimensional cavitation number. The authors carried out a numerical investigation into the dynamics of the transition between sheet and cloud cavitation regimes around the NACA0012 hydrofoil, in a study considering an oscillating hydrofoil. They used a barotropic law approach to numerically predict the cyclic transition between regimes at a large angle of attack. They concluded that the hydrofoil's main oscillation component has the same frequency as the shedding of a vapor cloud.

Large Eddy Simulation (LES) has been extensively used in recent works to investigate cavitation dynamics of fluid around hydrofoils. In [13], the authors investigated unsteady sheet-cloud cavitating flow around a twisted 3-D NACA foil, using LES and VOF techniques. They illustrated the detailed dynamics of cavitation evolution by depicting cavity growth, shedding and downstream collapse. The radial and lateral jet flows concerning the three-dimensional effects of a twisted wing were also reported. In [14], the authors studied the dynamic characteristics of cavitating flow around a sinusoidal wavy leading edge hydrofoil with a NACA 634-021 profile by means of multiphase modeling. They found that the geometrically modified hydrofoil, named the Wavy Leading Edge (WLE) hydrofoil, exhibits a significantly reduced level of unsteady fluctuations in dynamic forces.

Therefore, this paper proposes a new optimization procedure for the geometric definition of rotor blades free of cavitation applied to DAHTs. The main contribution of this work is the demonstration that η_d and C_{Td} can strongly impact the cavitation condition on a DAHT. Additionally, the proposed optimization can correct the chord and twist angle distributions, avoiding cavitation inception. The minimum pressure coefficient is used as the criterion to avoid cavitation in the BEMT model. A hydrokinetic turbine with a 10 m diameter was used to evaluate the effects of those diffuser parameters concerning cavitation. Comparisons with other models available in the literature are addressed. CFD calculations were carried out to investigate water vapor pressure over cavitating blades.

As a result, the proposed model shows that cavitation can increase under the effect of a diffuser, suggesting that such a phenomenon needs to be considered in the design of DAHT. In addition, the optimization method corrects the blade chord distribution, reducing the cavitation inception at the design condition when comparing the water vapor production rate for both corrected and uncorrected blade geometries. Even though it requires experimental validation, it is expected that the proposed methodology can be used in real applications.

This paper is organized as follows. The next section shows the optimization model for DAHTs. Section 3 presents the CFD methodology using the Rayleigh–Plesset cavitation model. In Section 4, the results and discussion are stated. Section 5 shows the conclusions of this study.

2. The Optimization for Hydrokinetic Blades Shrouded by Diffuser

2.1. Cavitation Criterion on Hydrokinetic Rotors

According to [15,16], cavitation is a major problem for horizontal axis marine current turbines, usually leading to vibration, blade surface damage and performance loss, mainly for large and medium rotors, where the relative velocities are higher. These issues need to be considered in the early stages of hydro rotor projects [7]. During the third regime of liquid flows (cavity flows [17]), a large amount of liquid vaporizes, forming vapor bubbles which make pressure and velocity fields significantly different from those in non-cavitating flows. The condition for cavitation to occur is that the local pressure p should have dropped to below the vapor pressure of water. For shrouded hydrokinetic rotors, the diffuser increases the flow axial velocity at the rotor plane. This characteristic can lead to a severe cavitation condition, having increasing adverse effects on the lift force generated at the blades. In non-cavitating flows, the cavitation criterion that relates the cavitation number σ and the minimum pressure coefficient c_{pmin} should be $c_{pmin} + \sigma \geq 0$, where c_{pmin} is the minimum value of the pressure coefficient c_p , defined by

$$c_p = \frac{p - p_{atm}}{\frac{1}{2}\rho W^2}, \quad (1)$$

where ρ is the fluid density, p and p_{atm} are the local and atmospheric pressures, respectively, and the relative velocity of water on each blade section is defined by [2] as

$$W = \sqrt{[V_0(1 - a_b)]^2 + [\Omega r(1 + a'_b)]^2}, \quad (2)$$

where V_0 is the free-stream velocity. The parameters a_b and a'_b are the axial and tangential induction factors at the blades, respectively, while Ω and r are the angular velocity and radial position of the turbine. The expression for the number of cavitation, σ , is described by [7] as:

$$\sigma = \frac{p_{atm} + \rho gh - p_v}{\frac{1}{2}\rho W^2}, \quad (3)$$

where g is the gravitational acceleration, h is the submerged distance and p_v is the vapor pressure. Another way to consider the cavitation at each blade section of a rotor is through Equation (4) [7], where the cavitation velocity is

$$V_{CAV} = \sqrt{\frac{p_{atm} + \rho gh - p_v}{-\frac{1}{2}\rho c_{pmin}}}. \quad (4)$$

V_{CAV} denotes the minimum flow velocity at which cavitation will occur for a specific radial position on the hydrokinetic blade, i.e., $V_{CAV} \geq W$. Figure 1 illustrates the static pressure condition on a DAHT blade section.

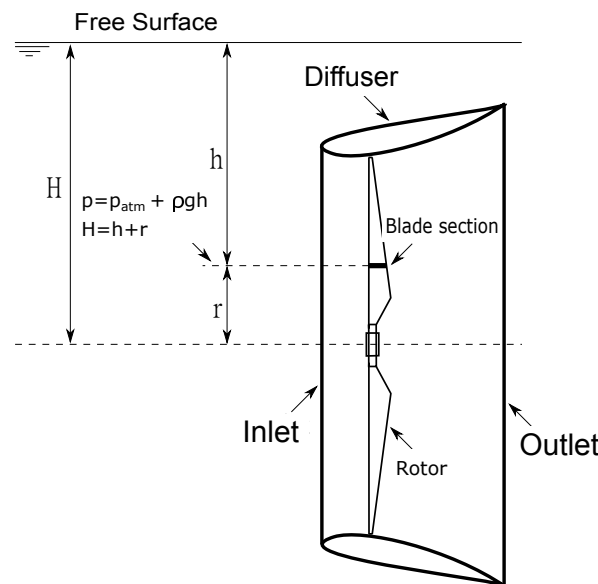


Figure 1. Static pressure condition on a DAHT blade section.

2.2. The Optimization Model

As reported in [18], to model a diffuser with losses, an approach similar to that used to determine duct flow in the presence of losses is required. It is assumed that the fluid surrounding the rotor is frictionless, and the rotational velocity component is ignored. The dashed lines in Figure 2 show the control volume used to analyze diffuser-augmented turbine performance. The optimum expressions for shrouded turbines come from the momentum equations with rotational velocities in the flow [4,19]. According to [20], for modern turbines, it is necessary to consider the effect of the tangential induction factor, a' . The elemental torque can be obtained directly from the momentum equation applied to the control surface shown in Figure 2, in which the infinitesimal area at the rotor plane is $dA = 2\pi r dr$, allowing the power coefficient as [18].

$$C_P = \varepsilon_1 \left[1 - \varepsilon_4^2 - (1 - \eta_d) (1 - \beta^2) \varepsilon_1^2 \right], \quad (5)$$

where V_4 is the velocity in the far-wake, $\varepsilon_4 = V_4/V_0$ is the dimensionless far-wake velocity, $\varepsilon_1 = V_1/V_0$ is the velocity ratio, and $V_1 = V_2$ the velocity at the rotor plane. $\beta = A/A_3$,

where A is assumed equal to the diffuser area at the rotor, A_3 is the cross-sectional area of the diffuser outlet and η_d is the diffuser efficiency. For a shrouded rotor, the power coefficient can be written using the pressure coefficient, c_{p3} , at the diffuser outlet, which is defined as

$$c_{p3} = \frac{p_3 - p_0}{\frac{1}{2}\rho V_0^2}, \quad (6)$$

where p_0 is the static pressure in the freestream. The thrust is obtained by dividing C_P by ε_1 , resulting in $C_T = C_P/\varepsilon_1$ [21]. C_P , C_T and c_{p3} strongly depend on ε_4 , as demonstrated by [22,23]. In [18], an expression for ε_4 was demonstrated by applying the momentum equation to the control volume shown in Figure 2, resulting in

$$\varepsilon_4 = \varepsilon_1 - \sqrt{(1 - \varepsilon_1)^2 + C_{Td} - \varepsilon_1^2(1 - \beta^2)(1 - \eta_d)}, \quad (7)$$

where C_{Td} is the diffuser thrust coefficient, which is important even if there were no losses in the diffuser ($\eta_d = 1$). Note further that solving Equations (5) and (6), and making $C_T = C_P/\varepsilon_1$ for the turbine thrust coefficient in terms of ε_4 , yields:

$$C_P = 2\varepsilon_1^2 \left[1 - \varepsilon_1 + \sqrt{(1 - \varepsilon_1)^2 + C_{Td} - \varepsilon_1^2(1 - \beta^2)(1 - \eta_d)} - \frac{C_{Td}}{2\varepsilon_1} \right], \quad (8)$$

$$c_{p3} = \varepsilon_1^2 (2 - \beta^2) - 2\varepsilon_1 \left[1 + \sqrt{(1 - \varepsilon_1)^2 + C_{Td} - \varepsilon_1^2(1 - \beta^2)(1 - \eta_d)} \right] + 1 + C_{Td} - \varepsilon_1^2(1 - \beta^2)(1 - \eta_d), \quad (9)$$

and

$$C_T = 2\varepsilon_1 \left[1 - \varepsilon_1 + \sqrt{(1 - \varepsilon_1)^2 + C_{Td} - \varepsilon_1^2(1 - \beta^2)(1 - \eta_d)} - \frac{C_{Td}}{2\varepsilon_1} \right]. \quad (10)$$

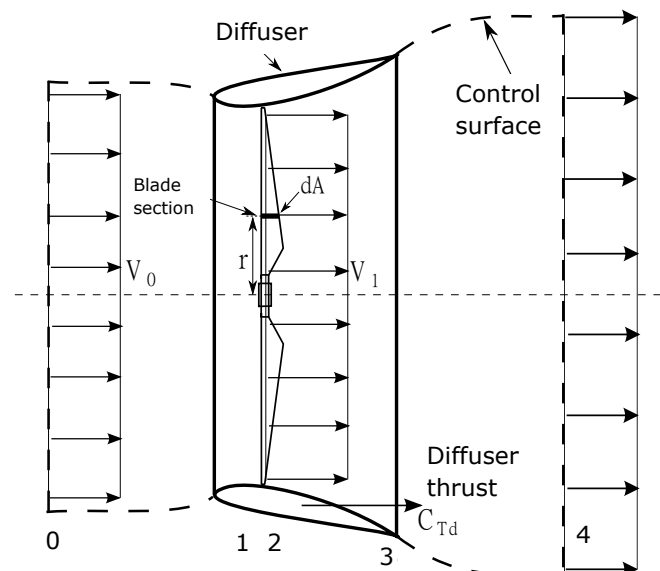


Figure 2. Simplified illustration of the flow velocities through an ideal DAHT. Control volume locations are: (0), free flow; (1) and (2), rotor plane; (3), diffuser end; and (4), far-wake.

The optimum values for ε_1 and ε_4 are determined by maximizing C_P in Equation (5), giving [18]:

$$6\varepsilon_{1opt}^3 \left[\beta^2(1 - \eta_d) + \eta_d \right] - C_{Td}\Delta + 4\varepsilon_{1opt}(1 + C_{Td} + \Delta) - 2\varepsilon_{1opt}^2(5 + 3\Delta) = 0, \quad (11)$$

where $\varepsilon_{1_{opt}} = 1 - a_{b_{opt}}$ and

$$\Delta = \sqrt{1 + C_{Td} + \varepsilon_{1_{opt}} \left\{ -2 + \varepsilon_{1_{opt}} [\beta^2(1 - \eta_d) + \eta_d] \right\}}. \quad (12)$$

Only the diffuser effect is considered in this optimization procedure, via three important parameters: η_d , β and C_{Td} . After determining $\varepsilon_{1_{opt}}$, the far-wake velocity, $\varepsilon_{4_{opt}}$, is calculated using Equation (7). On an annular control volume at radius r , considering the non-dependency of diffuser thrust, the elemental thrust coefficient is:

$$\frac{dC_T}{dr_*} = 4\varepsilon_1(1 - \varepsilon_4)r_*, \quad (13)$$

where $r_* = r/R$. The Prandtl tip loss factor, F , is included in ε_4 from Equation (7) with $a = a_b F$ as the streamtube average, resulting in [18]

$$\varepsilon_4 = 1 - a_b F - \sqrt{(a_b F)^2 - (1 - a_b F)^2(1 - \beta^2)(1 - \eta_d) + C_{Td}}, \quad (14)$$

From the blade element theory, the elemental thrust coefficient at each blade section is

$$\frac{dC_T}{dr_*} = 2\varepsilon_1^2 \frac{\sigma_s C_n r_*}{\sin^2 \phi}, \quad (15)$$

where $\sigma_s = Nc/(2\pi r)$ is the local solidity, $C_n = C_l \cos \phi + C_d \sin \phi$ is the normal force coefficient and ϕ the flow angle (Figure 3), defined as

$$\phi = \tan^{-1} \left[\frac{1 - a_b}{x(1 + a'_b)} \right], \quad (16)$$

where $x = \Omega r/V_0$. Therefore, from [5] the optimum corrected chord, c_{opt}^{co} , for each blade section is given by:

$$c_{opt}^{co} = c_{opt}^{uc} \left[\frac{W}{(1 - f_s)V_{CAV}} \right]^2, \quad (17)$$

where f_s is a safety factor, and c_{opt}^{uc} is

$$c_{opt}^{uc} = \frac{4\pi r_* (1 - \varepsilon_{4_{opt}}) \sin^2 \phi}{NC_n \varepsilon_{1_{opt}}}. \quad (18)$$

The correction on chord distribution is important because the diffuser increases the axial velocity at the rotor plane, consequently increasing the angle of attack, making cavitation relevant to be accounted for through the condition, $W \geq V_{CAV}$.

Equation (17) is the same as for a bare turbine. This is an interesting result because it is obtained by [7] for hydrokinetic turbines with no diffuser, demonstrating that, even for shrouded turbines, the term $\left[\frac{W}{(1 - f_s)V_{CAV}} \right]^2$ can be applied to correct the optimum chord distribution in order to avoid cavitation. After obtaining $\varepsilon_{1_{opt}}$ from Equation (11), the optimized a_{opt} can be easily calculated using $a_{b_{opt}} = 1 - \varepsilon_{1_{opt}}$. The tangential induction factor, a' , as a function of $\varepsilon_{1_{opt}}$ is found using conservation of energy, resulting in the optimum element power:

$$dP_{opt} = \frac{1}{2} \rho V_0^3 \left[\varepsilon_{1_{opt}} (1 - \varepsilon_{4_{opt}}^2) - \varepsilon_{1_{opt}}^2 (1 - \beta^2) (1 - \eta_d) \right] dA. \quad (19)$$

Additionally, applying the angular momentum equation to a blade section,

$$dP_{opt} = 2\rho V_0 a'_b \varepsilon_{1_{opt}} \Omega^2 r^2 dA. \quad (20)$$

Equations (19) and (20) give

$$a'_{b_{opt}} = \frac{2\varepsilon_{1_{opt}}(1 - \varepsilon_{4_{opt}}) - C_{Td}}{4x^2}, \quad (21)$$

with $\varepsilon_{4_{opt}}$ given by

$$\varepsilon_{4_{opt}} = \varepsilon_{1_{opt}} - \sqrt{(1 - \varepsilon_{1_{opt}})^2 + C_{Td} - \varepsilon_{1_{opt}}^2(1 - \beta^2)(1 - \eta_d)}. \quad (22)$$

Hence, the optimum flow angle, ϕ_{opt} , can be determined through Equation (16). To compute a given DAHT blade free of cavitation, the methodology is described in the Algorithm 1, in which the procedure for the calculation of the optimum chord and twist angle at each radius is shown.

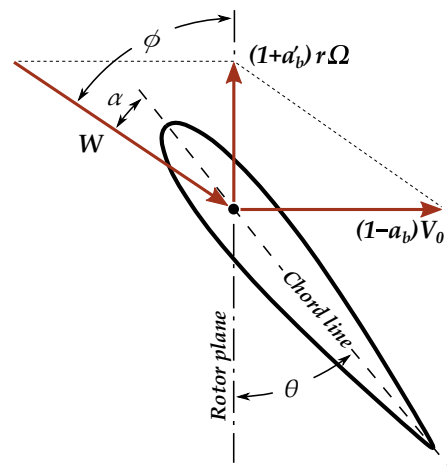


Figure 3. Blade element velocity diagram.

Algorithm 1 Chord and twist angle optimization

Require: $r, \Omega, C_L(\alpha_{opt}), C_D(\alpha_{opt})$ and V_0
for $i = 1$ to N_s (Number of sections) **do**
 Compute $a_{b_{opt}}$ and $a'_{b_{opt}}$ using Equations (11) and (21), respectively;
 Compute ϕ_{opt} using Equation (16) for $a_{b_{opt}}$ and $a'_{b_{opt}}$;
 Compute $C_n = C_l \cos \phi + C_d \sin \phi$, calculated for α_{opt} obtained from maximum C_l/C_d ;
 Compute the relative velocity, W ;
 Compute c_{opt}^{uc} , using Equation (18) and $\theta_{opt} = \phi_{opt} - \alpha_{opt}$;
 Compute V_{CAV} , using Equation (4);
 if $W > V_{CAV}$ **then**
 Compute c_{opt}^{co} , using Equation (18) or (17)
 end if
end for
Compute blade geometry.

3. Computational Fluid Dynamics Methodology

A numerical simulation using CFD (ANSYS-CFX) was carried out to investigate the flow through the DAHT to verify the occurrence of cavitation on the rotor blades, comparing the simulation to the results presented by [2,7]. Continuity and incompressible three-dimensional Reynolds-Averaged Navier–Stokes equations (RANS) are solved with the two equations $k-\omega$ SST turbulence model.

CFD simulation has been considered in three different approaches. For the first case, only the bare diffuser is placed in the fluid domain and simulation is carried out in order to compare the diffuser speed-up ratio γ with the results presented by [24].

The second approach intends to validate the bare rotor's overall efficiency with the results presented by [7], including the cavitation phenomenon. The Rayleigh–Plesset cavitation model [25] is used.

Finally, the cavitation model is applied to a diffuser-augmented hydrokinetic turbine (diffuser and rotor) so that the effects of cavitation in the rotor power and thrust coefficients can be achieved. Optimized blade geometry obtained by the procedure described in Section 2.2 was also simulated. The moment of inertia of the turbine was not taken into account in this paper because it is not important for the runaway condition of the rotor. It only becomes relevant during turbine starting for a constant flow velocity, as pointed out in [26].

3.1. Diffuser Geometry

Diffuser-augmented turbines have been published mainly for wind rotors [27–29]. In the present work, the geometry is modeled with a conical diffuser that encloses the turbine rotor with $L_d/D_i = 1.425$ and $\phi_d = 4^\circ$, as shown in Table 1. Figure 4 shows an illustration of the diffuser geometry.

Table 1. Diffuser dimensions.

Parameter	Value
Inlet diffuser diameter (D_i)	10.50 m
Outlet diffuser diameter (D_e)	12.60 m
Diffuser upstream length (L_1)	3.700 m
Diffuser downstream length (L_2)	11.263 m
Diffuser total length (L_d)	14.963 m
Diffuser thickness (t_d)	4.0 mm
Opening angle (ϕ_d)	4.0 deg

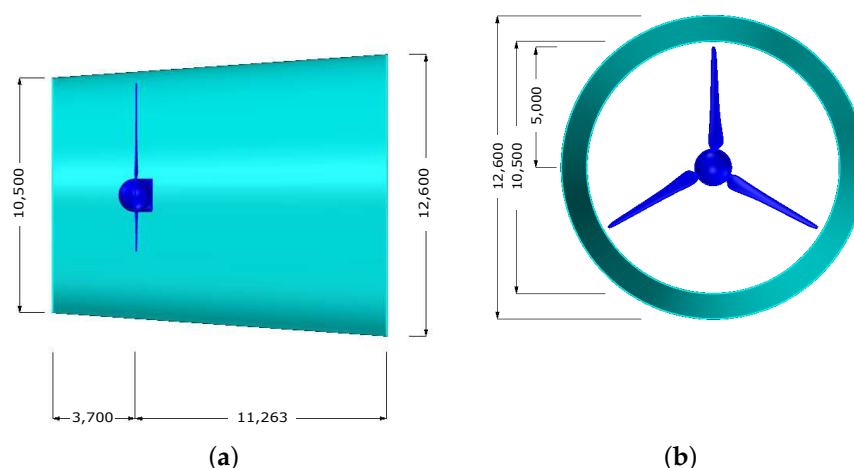


Figure 4. Diffuser geometry: (a) Centerline section view and (b) Front view. (Dimensions in mm).

3.2. Cavitating Flow Simulation

The fluid which passes through the diffuser-augmented hydrokinetic turbine is assumed to be incompressible and fully turbulent. The flow is three-dimensional, statistically stationary and represented by the Reynolds-Averaged Navier–Stokes (RANS) equations and the continuity equation in a finite volume scheme. This approach has been largely used to simulate wind turbines, as presented in [30]. Additionally, a similar CFD approach has been used to analyze the performance curve of a tidal current turbine [31].

The Reynolds Stress Tensor $\tau_{ij} = \rho \overline{u'_i u'_j}$ gives the contribution of the turbulent velocity fluctuations u'_i to the time-averaged velocity \bar{u}_i components and mean pressure \bar{p} [32].

Thus, the so-called k - ω Shear-Stress Transport (SST) model is applied [33]. This model has been developed to handle strong adverse pressure gradient flows so that it can predict the size and onset of flow separation caused by an adverse pressure gradient by calculating the transport of turbulence shear stress using an automatic wall treatment [31]. In this sense, the SST model is a natural choice for numerical simulation of flows through hydrokinetic turbines, which show physical similarity to wind turbines.

The cavitation process can be described by governing equations that assume a two-phase continuum mixture of liquid water and vapor. Thus:

$$\frac{\partial r_\alpha \rho_\alpha}{\partial t} + \frac{\partial r_\alpha \rho_\alpha \bar{u}_i}{\partial x_i} = \dot{m}_\alpha, \quad (23)$$

where ρ is the density and \dot{m}_α represents the rate of change of mass between the vapor and liquid phases, per unit of mixture volume.

$$\dot{m}_v = -\dot{m}_l. \quad (24)$$

The subscript $\alpha = (l, v)$ indicates the particular liquid or vapor phase, and r_α is the volume fraction scalar of each phase. With a thermal non-equilibrium approach between phases, the sum of the two volume fractions must equal one, i.e., $r_l + r_v = 1$ [34]. Assuming that both phases have the same velocity, the mean momentum conservation equation is derived by replacing the fluid density ρ with the mixture density $\rho_m = \rho_l r_l + \rho_v r_v$, as shown below

$$\rho_m \frac{\partial \bar{u}_j}{\partial t} + \rho_m \bar{u}_i \frac{\partial \bar{u}_j}{\partial x_i} = -\frac{\partial \bar{p}}{\partial x_j} + \frac{\partial}{\partial x_i} \left(2\mu S_{ij} - \rho_m \overline{u'_i u'_j} \right) + \rho_m f, \quad (25)$$

where μ is the dynamic viscosity, f is the additional momentum source (e.g., the gravitational, Coriolis and centrifugal forces). S_{ij} are the components of the symmetric part of the velocity gradient tensor. The Reynolds Stress Tensor $\rho_m \overline{u'_i u'_j}$ is supplied by the k - ω SST turbulence model.

Equation (24) allows the two-phase calculations to be performed by solving the continuity equation and the momentum equation written in the form of Equation (25). The rate of vapor production \dot{m}_v was calculated using the Rayleigh–Plesset Equation [25]. Thus, the dynamic growth of a spherical nucleated bubble can be described as:

$$R_B \frac{d^2 R_B}{dt^2} + \frac{3}{2} \left(\frac{dR_B}{dt} \right)^2 + \frac{2\sigma_{st}}{\rho_l R_B} = \frac{p_v - p}{\rho_l}, \quad (26)$$

where R_B is the radius of a nucleation site, σ_{st} is the surface tension coefficient, p_v is the pressure in the bubble, assumed to be the vapor pressure at liquid temperature, and p is the pressure outside the bubble.

Neglecting smaller bubbles and surface tension term as stated by [25], first-order approximation leads the Equation (26) to:

$$\frac{dR_B}{dt} = \sqrt{\frac{2}{3} \frac{p_v - p}{\rho_l}}. \quad (27)$$

Mass transfer needs to be modeled to describe the interphase mass transfer between vapor and liquid considering vaporization and condensation processes, respectively. Defining the bubble density number, N_B , as being the number of bubbles per unit of volume of the mixture (note that $m_v = \rho_v \frac{4}{3} \pi R_B^3$), the rate of change of vapor mass per unit of volume is:

$$\dot{m}_v = N_B \rho_v 4\pi R_B^2 \sqrt{\frac{2}{3} \frac{p_v - p}{\rho_l}}. \quad (28)$$

Equation (28), in terms of the vapor volume fraction $r_v = N_B 4\pi R_B^3/3$, is given by:

$$\dot{m}_v = \frac{3r_v\rho_v}{R_B} \sqrt{\frac{2}{3} \frac{p_v - p}{\rho_l}}. \quad (29)$$

Equation (29) only considers the vaporization, i.e., $\dot{m}_v > 0$, once $p_v - p$ is positive. Equation (29) cannot handle a radius decrease ($dR_B/dt < 0$) caused by condensation, when $p > p_v$. In addition, the original Rayleigh–Plesset model does not take into account the nucleation phenomena. Vaporization begins at nucleation sites and, as the vapor volume fraction increases, the nucleation site density decreases accordingly. Thus, in the expression for vaporization, r_v is replaced by $r_{nuc}(1 - r_v)$, where r_{nuc} is the volume fraction of the nucleation sites [35]. Finally, [36] proposed a modification that leads to Equation (30), where F_c is dimensionless empirical coefficient for both the condensation and vaporization processes.

$$\dot{m}_v = F_c \frac{3r_{nuc}(1 - r_v)\rho_v}{R_B} \sqrt{\frac{2}{3} \frac{|p_v - p|}{\rho_l}} \text{sgn}(p_v - p). \quad (30)$$

Coefficients of Equation (30) found by [36] are given in Table 2.

Table 2. Material constants and conditions for the Rayleigh–Plesset Model at 25 °C.

Quantity	Value
F_c	0.01 (Condensation) and 50 (Vaporization)
ρ_l	997 kg/m ³
ρ_v	0.02308 kg/m ³
r_{nuc}	5×10^{-4}
Mean bubble diameter (R_B)	1×10^{-6} m
Pressure of vapor (p_v)	3.170 kPa

3.3. Numerical Setup

The present work adopts a geometric model similar to that developed by [7] for cavitation study on the blade rotor. The blade geometry uses a NACA 65₃-618 foil whose distribution is described in Table 3. It is worth noting that NACA 65₃-618 was chosen only to assess the optimization process proposed here, and airfoil selection is not the focus of this study.

The computational domain is 31 m × 50 m × 150 m, as illustrated in Figure 5. The rotor is positioned at 2.5 D from the inlet boundary and 12.5 D to the outlet boundary. The diffuser and rotor center are located at 9 meters beneath the water’s surface ($H = 9$ m).

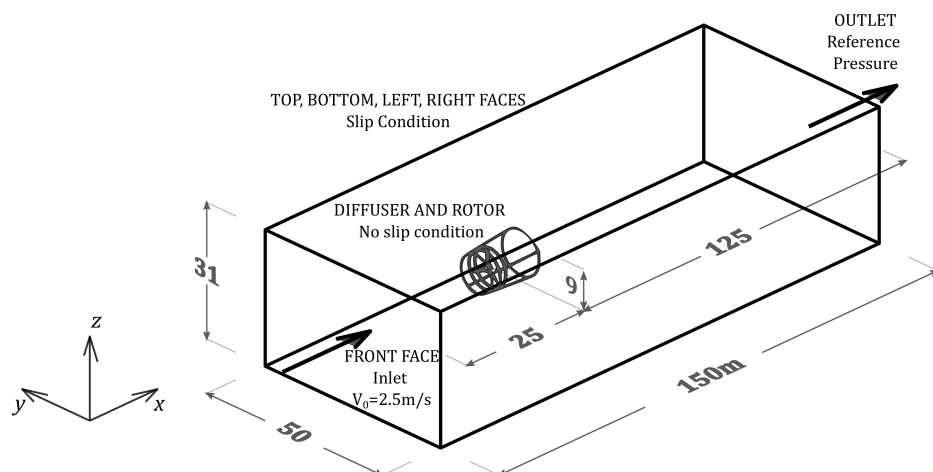


Figure 5. General setup of the computational domain and boundary conditions.

Table 3. Blade chord and twist distributions for the NACA 65₃-618 foil [7].

Radial Distance (<i>r</i>) [m]	Span Station (<i>r/R</i>) [–]	Chord Length [m]	Twist [deg.]	Twist Axis [% chord]
0.793	0.148	0.27	24	30
0.949	0.189	0.56	20	30
1.185	0.237	0.55	16	30
1.400	0.280	0.51	13	30
1.635	0.327	0.47	11	30
1.860	0.372	0.43	10	30
2.086	0.417	0.39	8	30
2.311	0.462	0.35	7	30
2.536	0.507	0.33	6	30
2.761	0.552	0.30	5	30
2.985	0.597	0.28	5	30
3.210	0.642	0.26	4	30
3.432	0.686	0.26	4	30
3.657	0.731	0.26	3	30
3.880	0.776	0.26	3	30
4.101	0.820	0.25	2	30
4.328	0.865	0.26	2	30
4.550	0.910	0.26	2	30
4.776	0.955	0.26	2	30
5.000	1.000	0.11	1	30

The boundary conditions are defined as follows. A uniform velocity (V_0) of 2.5 m/s and a turbulence intensity of 5% are applied at the inlet section as a Dirichlet boundary condition. At the outlet region, a pressure outlet boundary condition is specified with a constant static pressure over the boundary mesh face to prevent inflow from occurring. A non-slip condition is applied to the blades and diffuser surfaces. The free slip condition is satisfied at the top, bottom and lateral faces of the prismatic domain. An angular velocity of 35 revolutions per minute is imposed on the moving reference zone. The main parameters are given in Table 4. Boundary conditions are given in Table 5.

Table 4. Design parameters used in the simulation of the DAHT.

Parameter	Value
Turbine diameter (D)	10 m
Hub diameter	1.5 m
Number of blades (<i>N</i>)	3
Free stream velocity (V_0)	2.5 m/s
Water density (ρ) at 25 °C	997 kg/m ³
Submergence of the turbine (H)	9 m
p_{atm}	1 × 10 ⁵ Pa
p_v	3.17 × 10 ³ Pa
Gravity (g)	9.81 m/s ²
Angular velocity (Ω)	35 rpm
Foil type	NACA 65 ₃ -618

The domain was divided into three different zones: a thin cylindrical zone around the turbine rotor; a cylindrical zone that envelops the diffuser; and the remaining flow zone. All domains were defined as stationary except for a thin cylinder of 10.5 m in diameter and 2 m in length which encompasses the blades. Here, the domain was defined with respect to a moving reference frame where the governing equations are solved, taking into account the Coriolis and centrifugal forces components in the frozen rotor approach used by the CFD solver.

Table 5. Boundary conditions.

Region	Condition
Inlet	$V_0 = 2.50 \text{ m/s}$
Outlet	$p = \text{constant}$
Blade surface	No-slip
Rotor surface	No-slip
Top, bottom and lateral surfaces	Slip
Rotatory domain	Frozen rotor
Turbulence intensity	5%

Discretization of the fluid domain heavily interferes with the numerical solution and refinement must obey the importance of the region in the representation of the flow physics. In fact, the rotor wall, diffuser wall and diffuser interior are regions where mesh refinement must be performed with care in the present case. The resolution of the mesh in the boundary layer close to the rotor walls is still important due to the pressure drop at the suction side of the rotor blade and the consequent occurrence of cavitation when pressure is lower than vapor pressure at the nuclei of bubbles. According to the value of the parameter y^+ [37], defined as

$$y^+ = \frac{\Delta_y u^+}{\nu} \quad (31)$$

where u^+ is the wall shear velocity, Δ_y the wall distance, and ν the kinematic viscosity, the region close to the wall can be divided into three distinct layers: viscous layer ($y^+ < 5$), buffer layer ($5 < y^+ < 30$) and the fully turbulent layer ($y^+ > 30$) [38]. To accurately solve the viscous sublayer, the values of y^+ must be less than 5. In the present numeric model, the boundary layer near the rotor wall zone was defined using 25 cell elements, increasing the spatial scale by a factor of 1.2 between adjacent layers. The first mesh element was set to 10^{-6} m , resulting in a $y_{max}^+ = 1.01$, which is appropriate for the $\kappa - \omega$ SST turbulence model. The mesh distribution along the zones defined is shown in Figures 6–8.

Before all simulations, a mesh convergence study using 5 different meshes was conducted in order to verify the most appropriate distribution, number of cells, and nodes. In all meshes, the value of power and the y^+ variables were verified. This analysis discovered that a mesh with 20.5×10^6 cells exhibits no variation in these variables with further refinement, so this distribution was used in all simulations. More details about this evaluation are shown in Section 4.2.1.

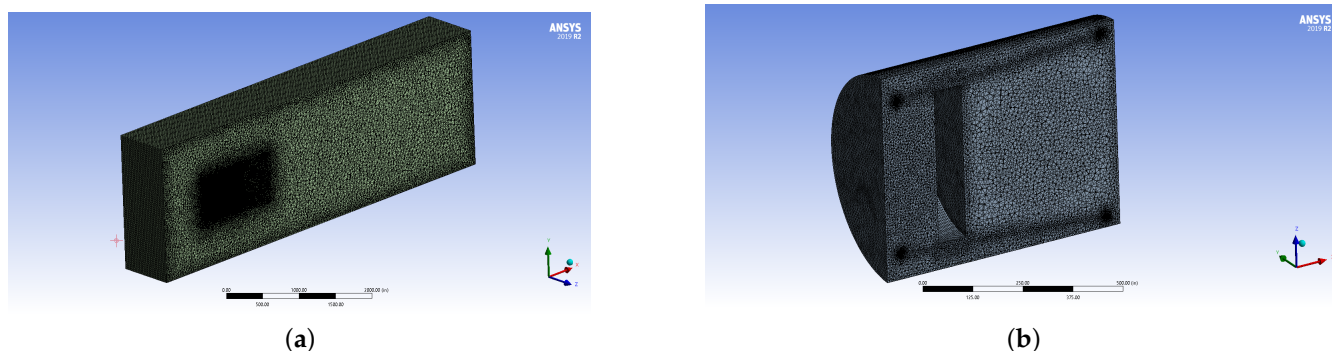


Figure 6. (a) Outer semi domain grid. Dark region in the center of the figure corresponds to the diffuser and rotor location. (b) Grid close to the diffuser (outer domain and MRF cylindrical meshes suppressed).

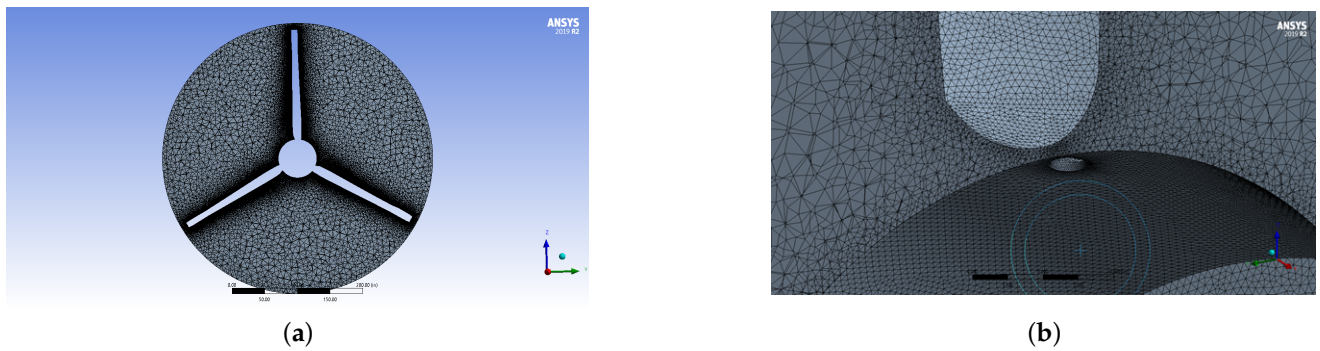


Figure 7. (a) Plan view in the cylindrical MRF grid surrounding the rotor. (b) 3-D close-up view near hub and blade.

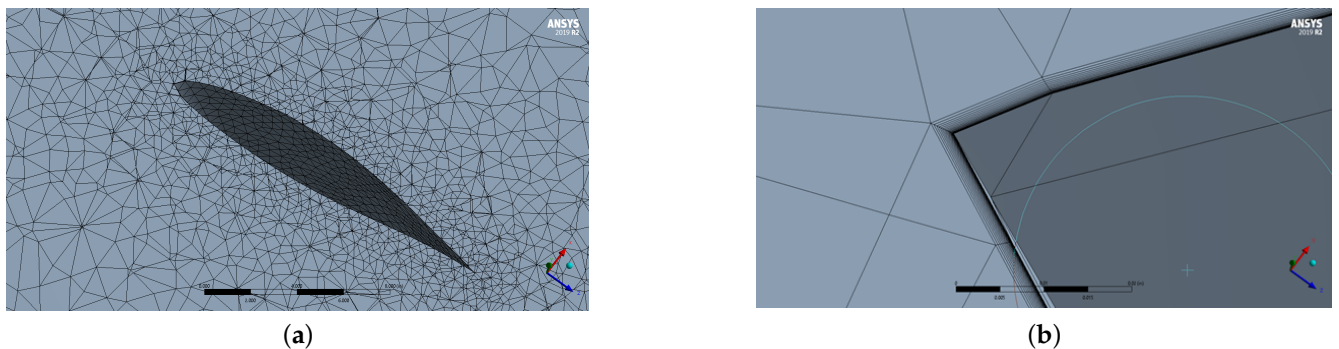


Figure 8. (a) View of the unstructured grid at a blade section. (b) Close-up view of the hydrofoil profile near the leading edge.

4. Results and Discussion

To assess the proposed optimization model, the design and geometric parameters shown in Tables 3 and 4 are used for all simulations. The results are divided into two phases: (i) the optimization model is evaluated considering the diffuser efficiency and thrust, and (ii) CFD simulations are performed to verify the optimization considering a model based on the volume fraction of water vapor.

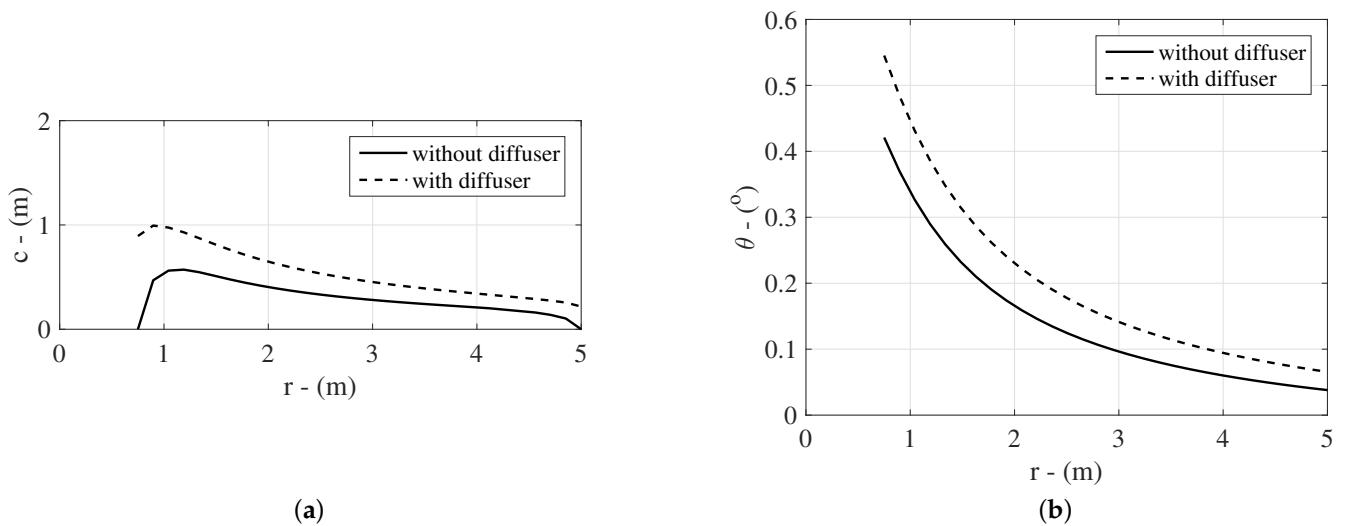
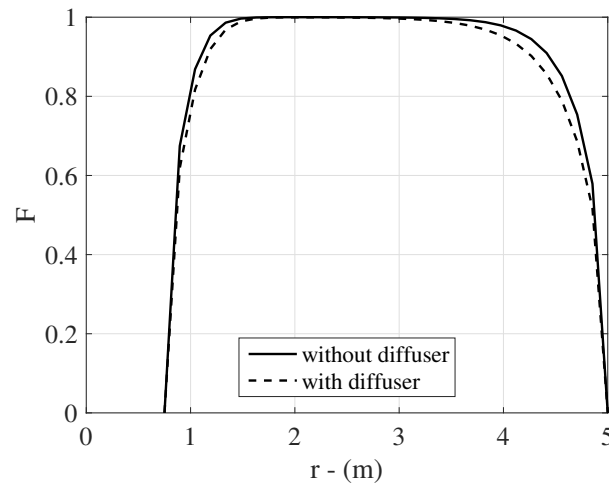
4.1. The Optimization Model

To analyze the optimization procedure with and without a diffuser, chord and twist angle distributions are presented in Figure 9. These results are obtained for a constant diffuser area ratio according to Table 6. The diffuser efficiency, area ratio and thrust shown in Table 6 are calculated from the dimensions and simulations made according to the computational methodology described in Section 3. The conical diffuser used here was chosen only for the purpose of evaluating the model's behavior. This work does not intend to analyze the variation of diffuser geometry.

Figure 9a shows that when the turbine is under the effect of a diffuser, the local chord does not tend to zero at the root and tip of the blade, as it is for a bare turbine case using Prandtl tip/root loss factor, F . In this case, the twist angle distribution is heavily impacted by the diffuser (Figure 9b). As recently pointed out by Vaz, Okulov and Wood [39], for a bare turbine optimization procedure using the Prandtl loss factor, the chord is always zero at the root and tip of the blade, as shown in Figure 10. This is because Equation (14) reduces the far wake velocity, ε_4 , to $\varepsilon_4 = 1 - a_b F$ for a bare turbine, and then, if $F \rightarrow 0$, $c \rightarrow 0$, as $\varepsilon_4 \rightarrow 1$. For a turbine with diffuser, the extra term in Equation (14), results in a value of ε_4 that is always less than unit, causing $c > 0$. This result demonstrates that, even when using tip loss models, any optimization that takes the diffuser effect into account, the chord will never be zero at root and tip of the blade. Consequently, the increased chord along the entire blade increases the torque produced by the rotor, which is important for starting the turbine, as starting behavior requires higher torque at low stream velocity [26,40].

Table 6. Diffuser design parameters.

Parameter	Value
β	0.7511
η_d	0.4712
C_{Td}	0.6458

**Figure 9.** (a) Chord and (b) twist angle distributions along the blade under the effect of a diffuser.**Figure 10.** Prandtl tip loss factor under the effect of a diffuser.

To assess the performance of the optimization procedure under cavitation conditions for a turbine with a diffuser, the design parameters shown in Table 4 are taken into account. The uncorrected and corrected chord distributions in relation to the cavitation are shown in Figure 11a. Note that cavitation occurs at approximately 80% of the blade length, and the model corrects the chord to avoid it. When W becomes higher than V_{CAV} , the model imposes a correction in order to modify the relative velocity, as shown in Figure 11b for radial positions $r > 4.12$ m. The method assumes W to always be lower than V_{CAV} . This optimization methodology is similar to that described in [5], with the main difference being the addition of diffuser efficiency and thrust into the mathematical approach, which is not reported in [5]. In the next section, CFD simulations are performed with optimized turbines with and without a diffuser.

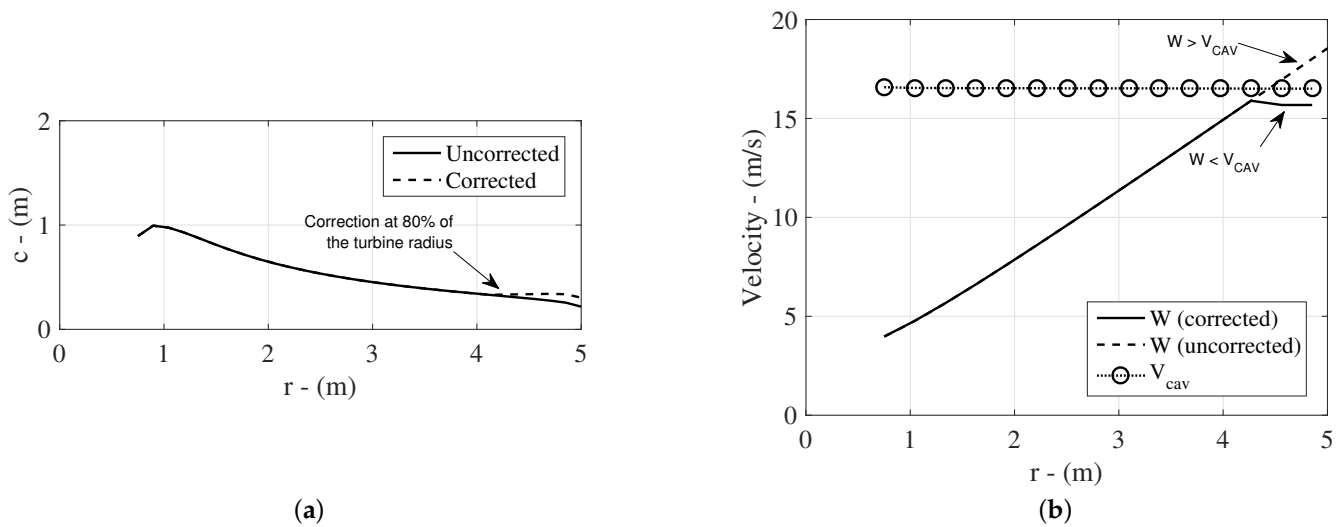


Figure 11. (a) Cavitation effect on the chord distribution along the blade. (b) Relative and cavitation velocities as functions of the radial position.

4.2. CFD Simulations and Validation

4.2.1. Verification of Optimal Point of Rotor Position and Mesh Independence Study

To ensure reliable and accurate results for the optimization model, mesh convergence studies and numerical validations must be carried out. The diffuser speed-up ratio obtained by CFD simulation was compared with experimental data obtained in [24]. Their measurements were performed with a 0.255-meter-long diffuser with a 0.5 mm thickness and a 5-degree opening angle. In the numerical model, the diffuser is empty; no rotational mesh has been implemented. The boundary layer near the rotor wall is defined with 25 layers, increasing by a factor of 1.2 between adjacent cells. The velocity ratio (V_x/V_0) in the diffuser centerline is depicted with the relative position (X/L_d) in Figure 12 and shows good agreement between the numerical and experimental results at the peak of the curve. This point is important because it is the location where the turbine is placed.

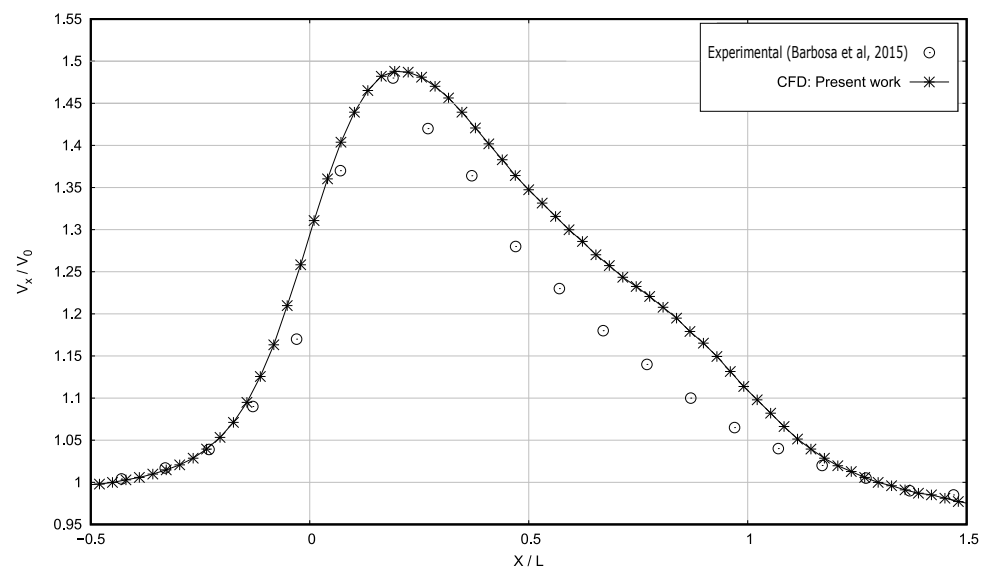


Figure 12. Comparative CFD-experimental velocity ratios on bare diffuser. Adapted from [24].

A grid refinement is applied in the interior and surrounding regions of the diffuser, downstream and upstream of the rotor, to assess the mesh dependence. As shown in Table 7, although there is a difference of one million between Meshes D and E for the

shrouded case, there is no significant change in values of mechanical power, evidencing the independence of the grid from the numerical results.

Table 7. Grid independence results—shrouded turbine.

Mesh	Cells [$\times 10^6$]	y_{max}^+	Power
Mesh A	16.2	1.32	388 kW
Mesh B	17.6	1.01	337 kW
Mesh C	18.9	1.15	333 kW
Mesh D	19.4	1.10	325 kW
Mesh E	20.5	1.11	324 kW

4.2.2. Numerical Simulation of Cavitation Effect on Diffuser-Augmented Hydrokinetic Blades

The hydrokinetic energy of the water passing over the rotor is proportional to the mass flow. Shrouding the rotor with a diffuser is a common method to increase the axial velocity and, consequently, the turbine power coefficient. However, due to the change in speed and pressure fields, cavitation can occur and affect the performance of the rotor. Optimized blade geometry should be able to mitigate this prejudicial effect. As previously described, cavitation occurs when $c_{pmin} + \sigma < 0$. The bare and shrouded turbines were subjected to the cavitation criterion as a function of radial position, Table 8. Indeed, the bare condition shows that cavitation occurs beyond 3.50 m up to the tip of the blade. These results seem strictly consistent with those reported by [7]. For the case of shrouded turbine, cavitation begins earlier, from 3.00 m of the blade length up to the tip. Figure 13 shows the cavitation at the suction side of the upward blade of the rotor.

Table 8. Cavitation criterion at upward blade.

r [m]	Bare Turbine			Shrouded Turbine		
	W [m/s]	σ	c_{pmin}	W [m/s]	σ	c_{pmin}
1.00	4.4366	17.9746	−4.4438	4.8882	14.8072	−4.5960
1.25	5.2192	12.8085	−3.8261	5.6089	11.0903	−4.2369
1.50	6.0395	9.4309	−3.1398	6.3809	8.4489	−3.6099
1.75	6.8841	7.1554	−2.8491	7.1868	6.5652	−3.4404
2.00	7.7450	5.5713	−2.4387	8.0165	5.2003	−3.0272
2.25	8.6173	4.4344	−2.2454	8.8635	4.1915	−2.8229
2.50	9.4979	3.5959	−2.1149	9.7230	3.4313	−2.5876
2.75	10.3847	2.9625	−2.0876	10.5926	2.8474	−2.5156
3.00	11.2762	2.4740	−1.9430	11.4700	2.3911	−2.2933
3.25	12.1714	2.0904	−1.7277	12.3537	2.0292	−2.0685
3.50	13.0695	1.7843	−1.7887	13.2425	1.7379	−1.7737
3.75	13.9700	1.5365	−1.5611	14.1354	1.5008	−1.5322
4.00	14.8724	1.3336	−1.3559	15.0299	1.3058	−1.3339
4.25	15.7764	1.1654	−1.1897	15.9229	1.1441	−1.1691
4.50	16.6818	1.0247	−1.0465	16.8117	1.0089	−1.0314
4.75	17.5882	0.9060	−0.9224	17.6833	0.8963	−0.9166
5.00	18.4957	0.8049	−0.8194	18.5221	0.8026	−0.8180

As discussed in Section 3.2, the total vapor volume is used to quantify cavitation. In this way, cavitation occurs only when the volume fraction of vapor is greater than 0.01. For the bare turbine, the simulation indicates a vapor volume equal to 383.6 mL, while for the shrouded turbine, it indicates 779.2 mL. In other words, the numerical simulations show that the shrouded turbine produces twice the amount of vapor as compared to the bare turbine. Figure 14a shows the top blade region where cavitation occurs on the suction side of the bare turbine. Figure 14b shows the same region where cavitation occurs for the shrouded turbine. This increase in cavitation occurs because the blade optimized by [7] did

not consider the diffuser effect. This fact demonstrates the need to account for the changes promoted by the diffuser on the flow during the blade optimization process.

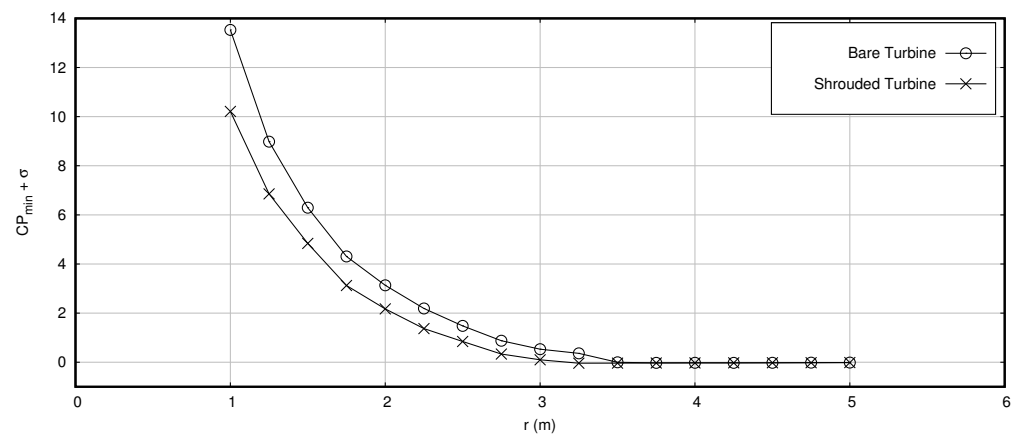


Figure 13. Cavitation criterion at upward blade (suction side).

The optimization due to the effect of the diffuser and cavitation correction were applied, as stated in Section 4.1, also shown in Figure 14c. The optimized blade was tested in the same simulation conditions applied to the previously shrouded configuration. It can be noticed that there is a complete absence of cavitation for the proposed optimized rotor blade. Note that the proposed methodology can integrally avoid cavitation inception. This occurs due to the optimization technique considering the increase in the axial velocity through the rotor blades, consequently increasing chord and twist angle distributions, as shown in Figure 9. This is a direct consequence of Equation (17), in which the chord is strongly dependent on the relative velocity, W .

After the correction of the blade geometry using the procedure shown in Section 2, the CFD simulation was carried out again, keeping the mesh distribution and data parameters used in Mesh E. In Figure 15, the pressure contour and streamlines for a shrouded, not corrected turbine are shown. Additionally, in Figure 16, the same data are shown for a shrouded turbine with blade correction. For a more detailed view of the pressure field in the fluid around the tip of the blade, a radial section at a radius $r = 4.9$ m was selected. These data are shown in Figure 17, for all cases studied. After blade geometry correction, no cavitation is found because the pressure values are all above the water vapor pressure.

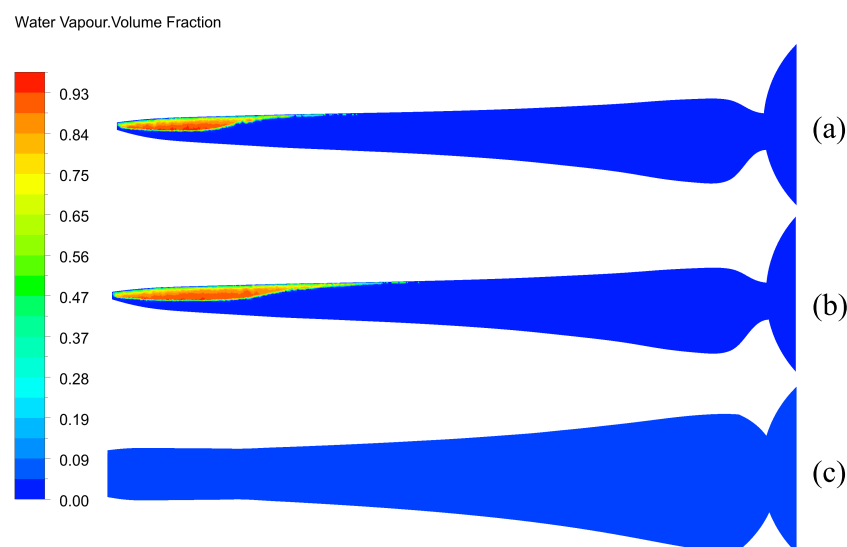


Figure 14. Volume fraction of water vapor at suction side: (a) bare turbine; (b) shrouded turbine; (c) corrected blade.

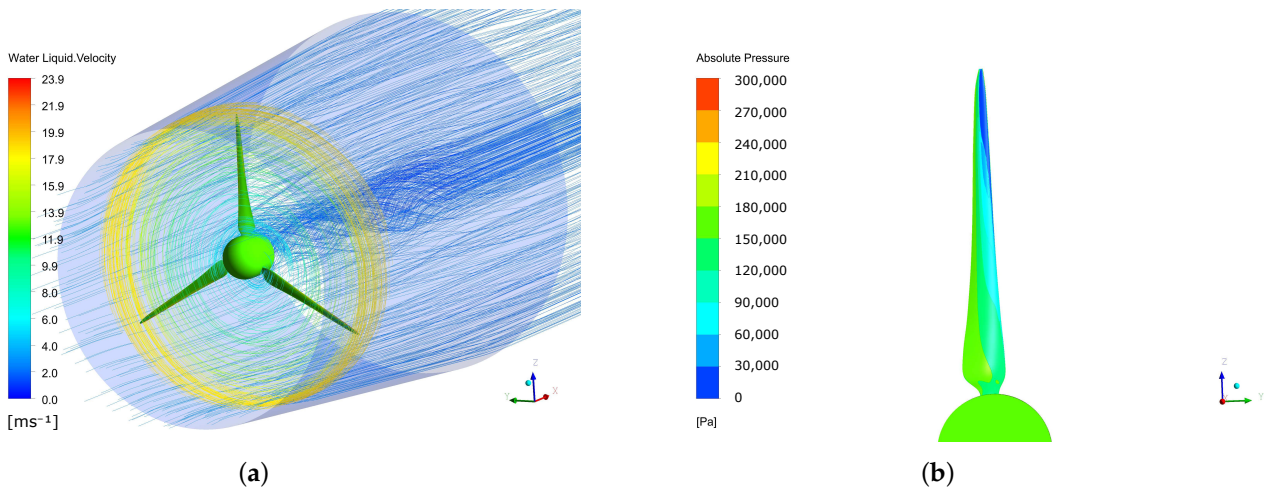


Figure 15. Streamlines colored by velocity magnitude and pressure contour in uncorrected blades surfaces. (a) Pressure side. (b) Suction side.

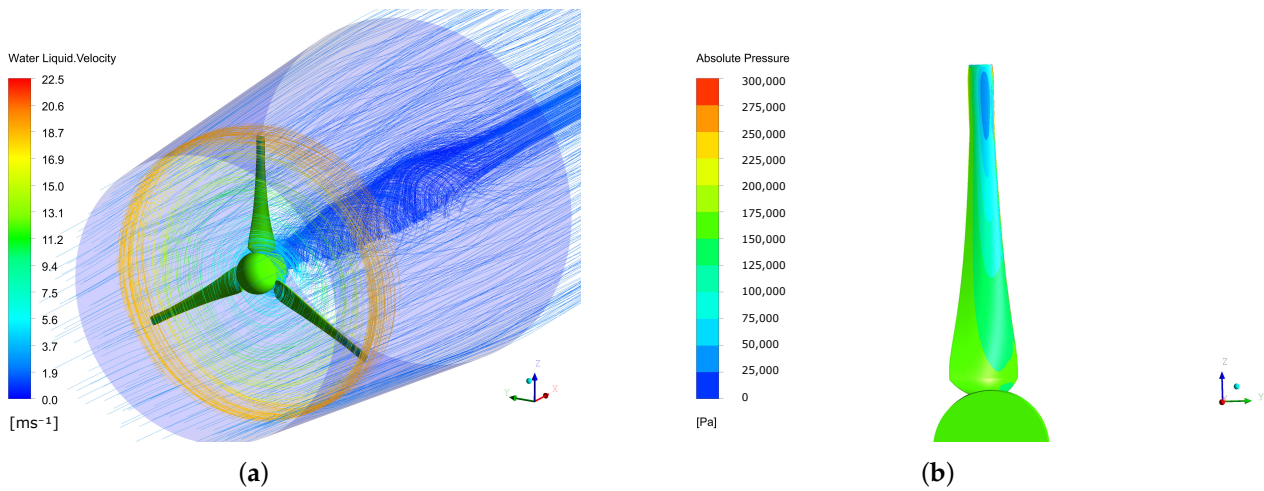


Figure 16. Streamlines colored by velocity magnitude and pressure contour in corrected blades surfaces. (a) Pressure side. (b) Suction side.

The power coefficient as a function of tip speed ratio, using BEMT, is shown in Figure 18. Note that the curve for C_p seems to be really flat when compared to that calculated by Silva et al. [7]. This behavior is also pointed out by [39], in which the authors suggest that diffuser-augmented wind turbines have much flatter power curves than bare turbines. This characteristic is important because it means that at any operating condition, a shrouded turbine tends to keep its efficiency higher.

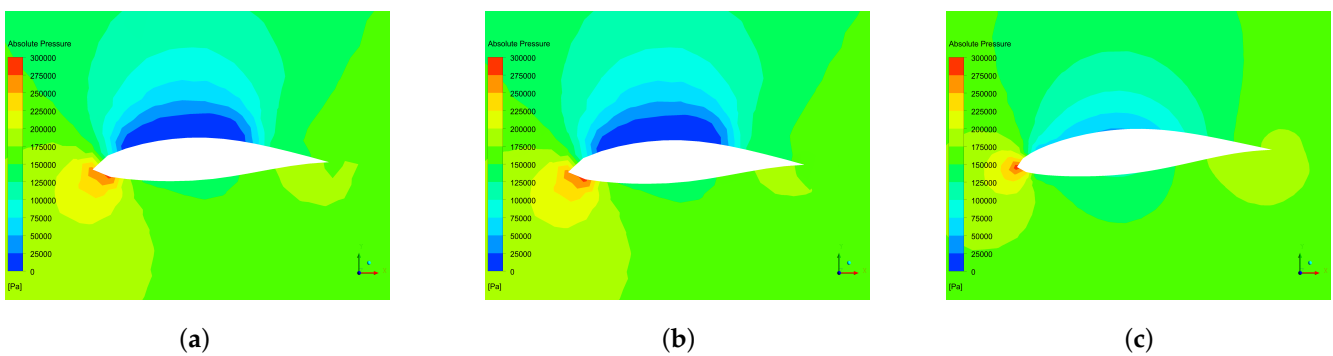


Figure 17. Pressure contour at a blade radius 4.9m from the rotor center. (a) Bare turbine. (b) Shrouded Turbine. (c) Shrouded optimized turbine.

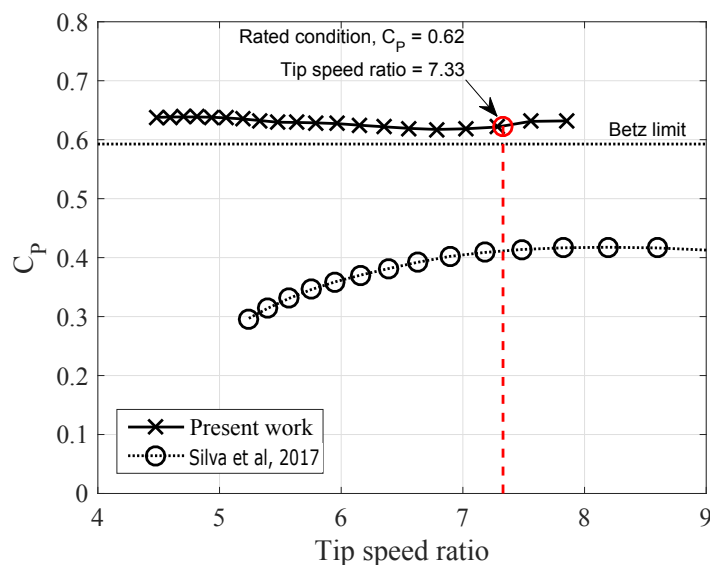


Figure 18. Power coefficient of the optimized blade with diffuser. Adapted from [7].

5. Conclusions

This work shows the development of a new optimization model applied to diffuser-augmented hydrokinetic blades, taking into account the effect of cavitation inception. The model demonstrates that diffuser efficiency, η_d , and thrust, C_{Td} , directly impact the cavitation on shrouded hydrokinetic blades. Such an impact occurs through the optimum expressions to calculate chord and twist angle, which are dependent on W^2 , as depicted in Equation (17). As shown in Figure 9, the optimization increases chord and twist angle distributions, altering the pressure condition at each blade section. To avoid cavitation inception, the results show that the model needs to account for the diffuser contribution to the flow passing through the rotor. As a result, the chord and twist angle change in order to keep the relative velocity W lower than the cavitation velocity V_{CAV} at all times. Another interesting result is that when the turbine is under the effect of a diffuser, the local chord does not tend to zero at the root and tip of the blade (Figure 9a), as it occurs for a bare turbine using the Prandtl tip/root loss factor, F , and the twist angle distribution is heavily impacted by the diffuser (Figure 9b). Even though the model presents good results, some limitations must be analyzed carefully. There is a need for model validation using experimental data, as well as analysis of the model in off-design conditions. Nevertheless, the work demonstrates that any optimization methodology needs to consider the diffuser as it can intensify the cavitation on hydrokinetic blades.

Author Contributions: Writing—review & editing, H.P.P., D.A.T.D.d.R.V., A.K.F.d.L., E.F.L. and J.R.P.V. All authors have read and agreed to the published version of the manuscript.

Funding: This research received no external funding.

Acknowledgments: The authors would like to thank ANTAQ, CNPq, CAPES, PROPESP/UFPA and PROCAD/UFPA project (no. 88881.200549/2018-01) for financial support.

Conflicts of Interest: The authors declare no conflict of interest.

Abbreviations

The following abbreviations are used in this manuscript:

BET	Blade Element Theory
CFD	Computational Fluid Dynamics
DAHT	Diffuser-augmented Hydrokinetic Turbine
DNS	Direct Numeric Simulation

HT	Hydrokinetic Turbine
MRF	Moving Reference Frame
LES	Large Eddy Simulation
RANS	Reynolds-Averaged Navier–Stokes
VOF	Volume Of Fluid Technique
Arabic Symbols	
a, a'	Streamtube average axial and tangential induction factors
a_b, a'_b	Axial and tangential induction factors at the blade
A	Area of the Disc (m^2)
A_3	Cross section at the diffuser outlet (m^2)
c	Chord (m)
c^{uc}, c^{co}	Uncorrected and corrected chord (m)
C_l, C_d	Lift and drag coefficients
C_p	Power coefficient
c_{p3}	Pressure coefficient at the diffuser outlet
c_{pmin}	Minimum pressure coefficient
C_n	Normal force coefficient
C_T, C_{Td}	Thrust coefficient and diffuser thrust coefficient
D	Turbine Diameter (m)
D_i, D_e	Inlet and outlet diffuser diameters (m)
dP	Elementary power (W)
f	Additional momentum source ($m\ s^{-2}$)
f_s	Safety factor
F	Prandtl's tip loss factor
F_c	Empirical constant of the cavitation model
g	Gravity ($m\ s^{-2}$)
h, H	Distance between free surface and turbine radial or center position (m)
\dot{m}_l, \dot{m}_v	Rate of change mass per unit of volume for liquid and vapor phases
L_1, L_2	Upstream and downstream diffuser lengths relative to rotor center plane (m)
L_d	Diffuser total length (m)
N	Number of blades
N_B	Number of bubbles per unit of mixture volume
p	Local pressure (Pa)
p_{atm}	Atmospheric pressure (Pa)
p_0	Pressure in the external flow (Pa)
p_2	Pressure in the turbine upstream (Pa)
p_3	Pressure in the diffuser outlet (Pa)
p_v	Vapor pressure (Pa)
r	Radial position at the rotor plane (m)
R	Radius of the rotor (m)
r_*	Dimensionless radial position
r_l, r_v	liquid and vapor volume fractions
r_{nuc}	Nucleation volume fraction
R_B	Bubble radius (m)
S_{ij}	Symmetric part of the velocity gradient tensor
u_i, u'_i	Mean velocity and fluctuations components ($m\ s^{-1}$)
$\overline{u'_i u'_j}$	Reynolds Stress Tensor ($m^2\ s^{-2}$)
t_d	Diffuser thickness (m)
V_x	X-component of the flow velocity at the diffuser centerline ($m\ s^{-1}$)
V_0	Freestream flow velocity ($m\ s^{-1}$)
V_1, V_2	Axial velocity at the rotor ($m\ s^{-1}$)
V_3, V_4	Axial velocity at the diffuser outlet and at the wake ($m\ s^{-1}$)
V_{CAV}	Minimum cavitating flow velocity ($m\ s^{-1}$)
X	Longitudinal position at the diffuser centerline (m)
W	Relative velocity of fluid

Greek Symbols

α	Angle of attack (rad)
β	Cross sectional area ratio
Δ_y	Wall distance (m)
ϵ_1	Velocity ratio
ϵ_4	Far-wake velocity ratio
η_d	Diffuser efficiency
γ	Diffuser speed-up ratio
μ	Dynamic viscosity ($\text{kg m}^{-1} \text{s}^{-1}$)
ν	Kinematic viscosity ($\text{m}^2 \text{s}^{-1}$)
Ω	Angular velocity of turbine (s^{-1})
ρ	Fluid density (kg m^{-3})
ρ_l, ρ_v, ρ_m	Liquid, vapor and mixture densities (kg m^{-3})
σ	Cavitation number
σ_s	Local solidity
σ_{st}	Surface tension coefficient
ϕ	Flow angle (rad)
ϕ_d	Diffuser opening angle
τ_{ij}	Reynolds stress tensor ($\text{m}^2 \text{s}^2$)
θ	Twist angle (rad)

Reference

- Mesquita, A.L.A.; Mesquita, A.L.A.; Palheta, F.C.; Vaz, J.R.P.; de Moraes, M.V.G.; Gonçalves, C. A methodology for the transient behavior of horizontal axis hydrokinetic turbines. *Energy Convers. Manag.* **2014**, *87*, 1261–1268. [[CrossRef](#)]
- Vaz, J.R.; Wood, D.H. Aerodynamic optimization of the blades of diffuser-augmented wind turbines. *Energy Convers. Manag.* **2016**, *123*, 35–45. [[CrossRef](#)]
- Zhu, F.w.; Ding, L.; Huang, B.; Bao, M.; Liu, J.T. Blade design and optimization of a horizontal axis tidal turbine. *Ocean Eng.* **2020**, *195*, 106652. [[CrossRef](#)]
- Silva, P.A.; Vaz, D.A.R.; Britto, V.; de Oliveira, T.F.; Vaz, J.R.; Junior, A.C.B. A new approach for the design of diffuser-augmented hydro turbines using the blade element momentum. *Energy Convers. Manag.* **2018**, *165*, 801–814. [[CrossRef](#)]
- do Rio Vaz, D.A.; Vaz, J.R.; Silva, P.A. An approach for the optimization of diffuser-augmented hydrokinetic blades free of cavitation. *Energy Sustain. Dev.* **2018**, *45*, 142–149. [[CrossRef](#)]
- Batten, W.; Bahaj, A.; Molland, A.; Chaplin, J. The prediction of the hydrodynamic performance of marine current turbines. *Renew. Energy* **2008**, *33*, 1085–1096. [[CrossRef](#)]
- Silva, P.A.S.F.; Shinomiya, L.D.; de Oliveira, T.F.; Vaz, J.R.P.; Mesquita, A.L.A.; Junior, A.C.P.B. Analysis of cavitation for the optimized design of hydrokinetic turbines using BEM. *Appl. Energy* **2017**, *185*, 1281–1291. [[CrossRef](#)]
- Taskar, B.; Steen, S.; Eriksson, J. Effect of waves on cavitation and pressure pulses of a tanker with twin podded propulsion. *Appl. Ocean. Res.* **2017**, *65*, 206–218. [[CrossRef](#)]
- Pennings, P.; Bosschers, J.; Westerweel, J.; van Terwisga, T. Dynamics of isolated vortex cavitation. *J. Fluid Mech.* **2015**, *778*, 288–313. [[CrossRef](#)]
- Wang, D.; Sampson, R. An experimental investigation on cavitation, noise, and slipstream characteristics of ocean stream turbines. *J. Power Energy* **2015**, *221*, 219–231. [[CrossRef](#)]
- Morgut, M.; Nobile, E.; Bilus, I. Comparison of mass transfer models for the numerical prediction of sheet cavitation around a hydrofoil. *Int. J. Multiph. Flow* **2011**, *37*, 620–626. [[CrossRef](#)]
- Chen, Y.; Chen, X.; Gong, Z.; Li, J.; Lu, C. Numerical investigation on the dynamic behavior of sheet/cloud cavitation regimes around hydrofoil. *Appl. Math. Model.* **2016**, *40*, 5833–5857. [[CrossRef](#)]
- Movahedian, A.; Pasandidehfarid, M.; Roohi, E. LES investigation of sheet-cloud cavitation around a 3-D twisted wing with a NACA 16012 hydrofoil. *Ocean Eng.* **2019**, *192*, 106547. [[CrossRef](#)]
- Pendar, M.R.; Esmailifard, E.; Roohi, E. LES study of unsteady cavitation characteristics of a 3-D hydrofoil with wavy leading edge. *Int. J. Multiph. Flow* **2020**, *132*, 103415. [[CrossRef](#)]
- Adhikari, R.C.; Vaz, J.; Wood, D. Cavitation inception in crossflow hydro turbines. *Energies* **2016**, *9*, 237. [[CrossRef](#)]
- Goundar, J.N.; Ahmed, M.R.; Lee, Y.H. Numerical and experimental studies on hydrofoils for marine current turbines. *Renew. Energy* **2012**, *42*, 173–179. [[CrossRef](#)]
- Lauterborn, W.; Ohl, C.D. Cavitation bubble dynamics. *Ultrason. Sonochem.* **1997**, *4*, 65–75. [[CrossRef](#)]
- Vaz, J.R.; Wood, D.H. Effect of the diffuser efficiency on wind turbine performance. *Renew. Energy* **2018**, *126*, 969–977. [[CrossRef](#)]
- Phillips, D.G. An Investigation on Diffuser Augmented wind Turbine Design. Ph.D. Thesis, University of Auckland, Auckland, New Zealand, 2003.
- do Rio, D.A.T.D.; Mesquita, A.L.A.; Vaz, J.R.P.; Blanco, C.J.C.; Pinho, J.T. An extension of the blade element momentum method applied to diffuser augmented wind turbines. *Energy Convers. Manag.* **2014**, *87*, 1116–1123.

21. Hansen, M.O.L.; Sørensen, N.N.; Flay, R. Effect of placing a diffuser around a wind turbine. *Wind Energy Int. J. Prog. Appl. Wind Power Convers. Technol.* **2000**, *3*, 207–213.
22. Sørensen, J.N. *General Momentum Theory for Horizontal Axis Wind Turbines*; Springer: Berlin/Heidelberg, Germany, 2016; Volume 4. [[CrossRef](#)]
23. Bontempo, R.; Manna, M. Effects of the duct thrust on the performance of ducted wind turbines. *Energy* **2016**, *99*, 274–287. [[CrossRef](#)] [[PubMed](#)]
24. Barbosa, D.; Vaz, J.; Figueiredo, S.; E Silva, M.; Lins, E.; Mesquita, A. An investigation of a mathematical model for the internal velocity profile of conical diffusers applied to DAWTs. *Ann. Braz. Acad. Sci.* **2015**, *87*, 1133–1148. [[CrossRef](#)]
25. Plesset, M.; Prosperetti, A. Bubble dynamics and cavitation. *Annu. Rev. Fluid Mech.* **1977**, *9*, 145–185. [[CrossRef](#)]
26. Vaz, J.R.; Wood, D.H.; Bhattacharjee, D.; Lins, E.F. Drivetrain resistance and starting performance of a small wind turbine. *Renew. Energy* **2018**, *117*, 509–519. [[CrossRef](#)]
27. Igra, O. Research and Development for Shrouded Wind Turbines. *Energy Convers. Manag.* **1981**, *21*, 13–48. [[CrossRef](#)]
28. Bet, F.; Grassmann, H. Upgrading conventional wind turbines. *Renew. Energy* **2003**, *28*, 71–78. [[CrossRef](#)]
29. Ohya, Y.; Karasudania, T.; Sakurai, A.; Abeb, K.I.; Inoue, M. Development of a shrouded wind turbine with a flanged diffuser. *J. Wind. Eng.* **2008**, *96*, 524–539.
30. Benjanirat, S.; Sankar, L.; Xu, G. Evaluation of turbulence models for the prediction of wind turbine aerodynamics. In Proceedings of the ASME 2003 Wind Energy Symposium, Reno, NV, USA, 6–9 January 2003; Paper number WIND2003-517; pp. 73–83.
31. Jo, C.; Yim, J.; Lee, K.; Rho, Y. Performance of horizontal axis tidal current turbine by blade configuration. *Renew. Energy* **2012**, *42*, 195–206.
32. Pope, S. *Turbulent Flows*; Cambridge University Press: Cambridge, MA, USA, 2000. [[CrossRef](#)]
33. Menter, F. Two-equation eddy-viscosity turbulence models for engineering applications. *AIAA J.* **1994**, *32*, 1598–1605.
34. Gerber, A. Two-equation eddy-viscosity turbulence models for engineering applications. In Proceedings of the ASME International Mechanical Engineering Congress & Exposition, New Orleans, LA, USA, 17–22 November 2002; Paper number IMECE2002-39315.
35. Morgut, M.; Nobile, E. Numerical Predictions of Cavitating flow around model scale propellers by CFD and advanced model calibration. *Int. J. Rotating Mach.* **2012**, *2012*, 618180. [[CrossRef](#)]
36. Bakir, F.; Rey, R.; Gerber, A.G.; Belamri, T.; Hutchinson, B. Numerical and experimental investigations of the cavitating behaviour of an inducer. *Int. J. Rotating Mach.* **2004**, *10*, 15–25.
37. Schlichting, H.; Gersten, K. *Boundary-Layer Theory*; Springer: Berlin/Heidelberg, Germany, 2000.
38. Wilcox, D.C. *Turbulence Modeling for CFD*, 3rd ed.; DCW Industries, Inc.: La Canada, CA, USA, 2006.
39. Vaz, J.R.; Okulov, V.L.; Wood, D.H. Finite blade functions and blade element optimization for diffuser-augmented wind turbines. *Renew. Energy* **2020**, *165*, 812–822
40. Moreira, J.L.; Mesquita, A.L.; Araujo, L.F.; Galhardo, M.A.; Vaz, J.R.; Pinho, J.T. Experimental investigation of drivetrain resistance applied to small wind turbines. *Renew. Energy* **2020**, *153*, 324–333.